ADVANCED FUNCTIONAL MATERIALS
www.afm-journal.de

Gas Adsorption Magnetic Variation Effect Enhanced Room-Temperature NO_2 Sensing with Fe_3GaTe_2

Jiangnan Chang, Minghao Zheng, Yifei Fan, You Wu, Ziru Zhang, Yancong Feng, Hao Li, Min Zeng, Yanan Guo, Meijin Zhang, Patrick J. French, Renfeng Dong, Zhipeng Hou, Guofu Zhou, and Yao Wang**

Achieving high-performance, low-power gas detection at room temperature is critical to safety and energy efficiency, and the key is to deeply explore the interaction mechanisms between sensitive materials and gases. In this work, a magnetic field-assisted strategy is developed to achieve high-performance, low-power NO_2 sensing with the Fe_3GaTe_2 at room temperature. Fe_3GaTe_2 nanoflakes are obtained from green solvents using ultrasound-assisted liquid phase exfoliation. The experimental results confirming that the Fe_3GaTe_2 nanoflakes sensor demonstrates an excellent response (S = 16 for 10 ppm NO_2, 1.4 times higher than that without magnetic field), a lower actual detection limit (50 ppb) and a low-power consumption (0.25 nW) under 21 mT magnetic field at room temperature. Combining theoretical calculations and quasi in situ XPS, it is indicated that Fe is the main electron donor and serves as the main response site for NO_2. Magnetic field-enhancing effect for gas sensing is revealed via comparing the in situ field-dependent magnetization curves of Fe_3GaTe_2 in air and NO_2. It is found for the first time that the enhancement of gas sensing is mainly attributed to the gas adsorption magnetic variation effect (GAMVE) which generates in NO_2. This study provides a strategy of GAMVE-driven sensing for next-generation gas sensors.

1. Introduction

With the advancement of the Internet of Things (IoT) and Artificial Intelligence (AI), utilizing smart devices for air quality monitoring and gas detection has evolved into a critical strategy for global environmental sustainability. Nitrogen dioxide (NO_2), as a ubiquitous and highly reactive gaseous pollutant mainly originating from fossil fuel combustion and automotive exhaust emissions, poses an escalating threat to environmental and public health.[1–3] Therefore, achieving high-performance detection of NO_2 at room temperature (RT) plays a crucial role.

In recent years, significant efforts have been devoted to enhancing gas-sensing performance through strategies leveraging intrinsic material properties[4,5] and external stimuli.[6,7] Thermal activation and photoexcitation, as prevalent external stimuli, have demonstrated remarkable efficacy in modulating gas-material interactions. Due to magnetism being an inherent fundamental property of materials, magnetic field regulation has been extensively studied in photocatalysis[8] and electrocatalysis,[9] presenting a highly promising strategy. Compared to other external fields, magnetic fields offer advantages including environmental friendliness, easy regulation, and relatively lower power consumption.[10] These attributes will contribute to enhancing the energy efficiency and power

J. Chang, M. Zheng, Y. Fan, Y. Wu, Z. Zhang, Y. Feng, H. Li, M. Zhang, Z. Hou, G. Zhou, Y. Wang
Guangdong Provincial Key Laboratory of Optical Information Materials and Technology
South China Academy of Advanced Optoelectronics
South China Normal University
Guangzhou 510006, P. R. China
E-mail: houzp@m.scnu.edu.cn; wangyao@m.scnu.edu.cn

J. Chang, Y. Fan, Y. Wu, Z. Zhang, Y. Feng, H. Li, M. Zeng, G. Zhou, Y. Wang
Institute of Electronic Paper Displays
National Center for International Research on Green Optoelectronics
South China Normal University
Guangzhou 510006, P. R. China

M. Zheng, Z. Hou
Institute for Advanced Materials
South China Academy of Advanced Optoelectronics
South China Normal University
Guangzhou 510006, P. R. China

Y. Guo
Southern Marine Science and Engineering Guangdong Laboratory (Zhuhai)
Zhuhai 519080, P. R. China

M. Zeng
National Key Laboratory of Advanced Micro and Nano Manufacture Technology Shanghai Jiao Tong University
Shanghai 200240, P. R. China

P. J. French
Bioelectronics Laboratory
EEMCS, TU Delft
Mekelweg 4, Delft 2628CD, The Netherlands

The ORCID identification number(s) for the author(s) of this article can be found under https://doi.org/10.1002/adfm.202526844

DOI: 10.1002/adfm.202526844

consumption ratio of sensors, while also facilitating more compact device integration. Consequently, magnetic field-assisted gas sensing has emerged as a burgeoning research focus. Recent studies indicate that magnetic fields can enhance gas sensing performance by inducing ordered magnetic moments and optimizing carrier transfer efficiency, offering new insights for designing next-generation gas sensors.[11–15] However, research on magnetic field-assisted gas sensing remains challenging, which lies in current studies predominantly rely on modifying inherently non-magnetic or paramagnetic materials using magnetic elements. In comparison, intrinsic magnetic materials offer significant advantages in delving into the underlying mechanisms by which magnetic fields influence gas sensing behavior.

2D materials have emerged as promising candidates for room-temperature gas sensing due to their large specific surface area, unique crystal structures, and distinctive physicochemical properties.[16,17] Most of traditional magnetic 2D materials do not show ferromagnetism at room temperature since their Curie temperatures are below room temperature. Hence, they could not be applied in room temperature gas sensing systems. The recently discovered 2D van der Waals intrinsic ferromagnetic material Fe_3GaTe_2 exhibits a Curie temperature higher than room temperature (Tc≈350–380 K), large saturation magnetization, and excellent electronic properties including high carrier mobility.[18–21] Endowed with these properties, Fe_3GaTe_2 emerges as not only a viable candidate for developing high-performance room-temperature gas sensing but also an optimal medium for further investigating the sensing mechanisms of magnetic-field influence.

In this study, we report the utilization of 2D van der Waals ferromagnetic Fe_3GaTe_2 for NO_2 sensing at room temperature. Bulk Fe_3GaTe_2 crystals were mechanically exfoliated by weakening interlayer van der Waals interactions without introducing intermediates, followed by ultrasound-assisted liquid-phase exfoliation in a water/ethanol mixed solvent to yield Fe_3GaTe_2 nanoflakes for NO_2 sensing at room temperature. A magnetic field-assisted strategy to achieve high-performance, low-power consumption NO_2 sensing with the Fe_3GaTe_2 nanoflakes at room temperature was further developed. The enhancement mechanism was proposed for the first time based on in situ magnetic field-dependent magnetization curves of Fe_3GaTe_2, revealing that the gas adsorption magnetic variation effect (GAMVE) generated in NO_2 is the primary cause of gas sensing enhancement. It provides a new perspective for exploring sensing mechanisms and the design of high-performance NO_2 sensors at room temperature.

R. Dong
School of Chemistry and Chemical Engineering
Key Laboratory of Clean Energy Materials Chemistry of Guangdong Higher Education Institutes
Lingnan Normal University
Zhanjiang 524048, P. R. China
R. Dong
School of Chemistry
South China Normal University
Guangzhou 510006, P. R. China

2. Results and Discussion

2.1. Sample Preparation and Characterization

Fe_3GaTe_2 nanoflakes were prepared via the liquid-phase exfoliation (LPE) method with a green solution. Reducing the thickness and lateral dimensions of the materials by grinding. Through ultrasonic treatment to weaken the interlayer van der Waals (vdW) force and widen the interlayer spacing for acquiring the exfoliated nanoflakes, and further freeze-drying to obtain powders for subsequent tests (**Figure 1**). The crystal structures of the materials were analyzed in **Figure 2a**. X-ray diffraction (XRD) analysis of Fe_3GaTe_2 crystals confirmed a centrosymmetric $P6_3/mmc$ space group, consistent with previous reports,[19] verifying the successful synthesis of Fe_3GaTe_2 crystals. The full width of the half-maximum of the (002) peak is 0.1°, indicating the good crystallinity and high-quality. The pattern of Fe_3GaTe_2 nanoflakes revealed reduced crystallinity and exposed more crystal planes compared to the crystal results, while matching the simulated XRD pattern.

The morphologies of the as-prepared Fe_3GaTe_2 before and after exfoliation are further characterized using scanning electron microscopy (SEM) and transmission electron microscopy (TEM). Figure S1 (Supporting Information) displays the SEM image of the bulk crystal before and during exfoliation, showing the large lateral dimensions and thickness. The typical EDX results shown the stoichiometry consistent with Fe_3GaTe_2 (Figure S2, Supporting Information). In contrast, the exfoliated nanoflakes exhibit significantly reduced dimensions and the morphology with the thickness of ≈6.86 nm (Figure 2b; Figure S3, Supporting Information). Additionally, EDS mapping demonstrated a homogeneous distribution of Fe, Ga and Te elements (Figure 2c). The surface composition and chemical states of Fe_3GaTe_2 were characterized by X-ray photoelectron spectroscopy (XPS). As shown in Figure 2d, the high-resolution Fe 2p spectrum was deconvoluted into Fe $2p_{3/2}$ and Fe $2p_{1/2}$ components. The peaks at 707.1 and 720.9 eV originate from metallic iron (Fe^0) in Fe_3GaTe_2. The additional doublet peaks at 711.5 and 725.2 eV correspond to Fe^{3+} species. Similarly, the Te 3d spectrum (Figure 2e) was deconvoluted into Te $3d_{5/2}$ and Te $3d_{3/2}$ peaks located at 573.1 and 583.4 eV, respectively, confirming the presence form of Te^{2-} species.[21] As displayed in Figure 2f, Raman spectroscopy of Fe_3GaTe_2 crystals revealed two characteristic phonon modes at 122.7 cm^{-1} ($A_{1g}{}^1$) and 140.3 cm^{-1} ($E_{2g}{}^2$).[22] In contrast, the nanoflakes sample exhibited a red-shift in $A_{1g}{}^1$ and $E_{2g}{}^2$ to 120.7 and 138.3 cm^{-1}, indicating a reduction in vibrational energy. This red shift is attributed to weakened van der Waals interactions and increased structural disorder, and it may also be accompanied by the formation of vacancies,[23] consistent with the other results of exfoliated Fe_3GaTe_2.

2.2. Gas Sensing Performance

To investigate the effect of magnetic field on the gas sensing properties, it is first necessary to study the gas sensing performance of the samples without an applied magnetic field. At room temperature, the response characteristics of the sensor to NO_2 gas without a magnetic field were investigated. Upon introduction of NO_2, the resistance of the sensor instantaneously decreased

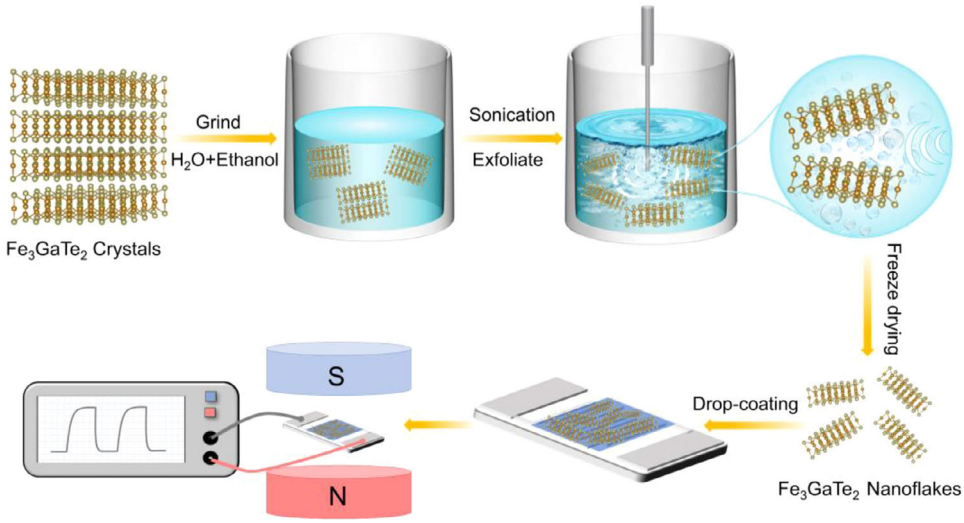

Figure 1. Schematic diagram of the liquid-phase exfoliation method and the gas sensing measuring system.

and remained stable in the NO_2 atmosphere. When NO_2 was released, the resistance could return to the initial value, exhibiting a typical p-type sensing curve and full recoverability. The sensor demonstrated a response of 11.25 to 10 ppm NO_2, as shown in Figure S4a (Supporting Information). Meanwhile, **Figure 3**a displayed a stable response curve over five consecutive test cycles, indicating remarkable cyclic stability. The sensor was tested with 0.1–15 ppm NO_2 (Figure 3b), showing a typical response increase with increasing gas concentration and a well-fitted linear relationship (Figure S4b, Supporting Information). The lowest actual detected concentration can be as low as 0.1 ppm, and the response could reach 1.23, which is capable of detecting the limit concentration set by European Union for protecting public health and the environment (200 μg m^{-3}).[24] These results demonstrate that the sensor exhibits stable and excellent room-temperature sensing capability for NO_2 without an applied magnetic field.

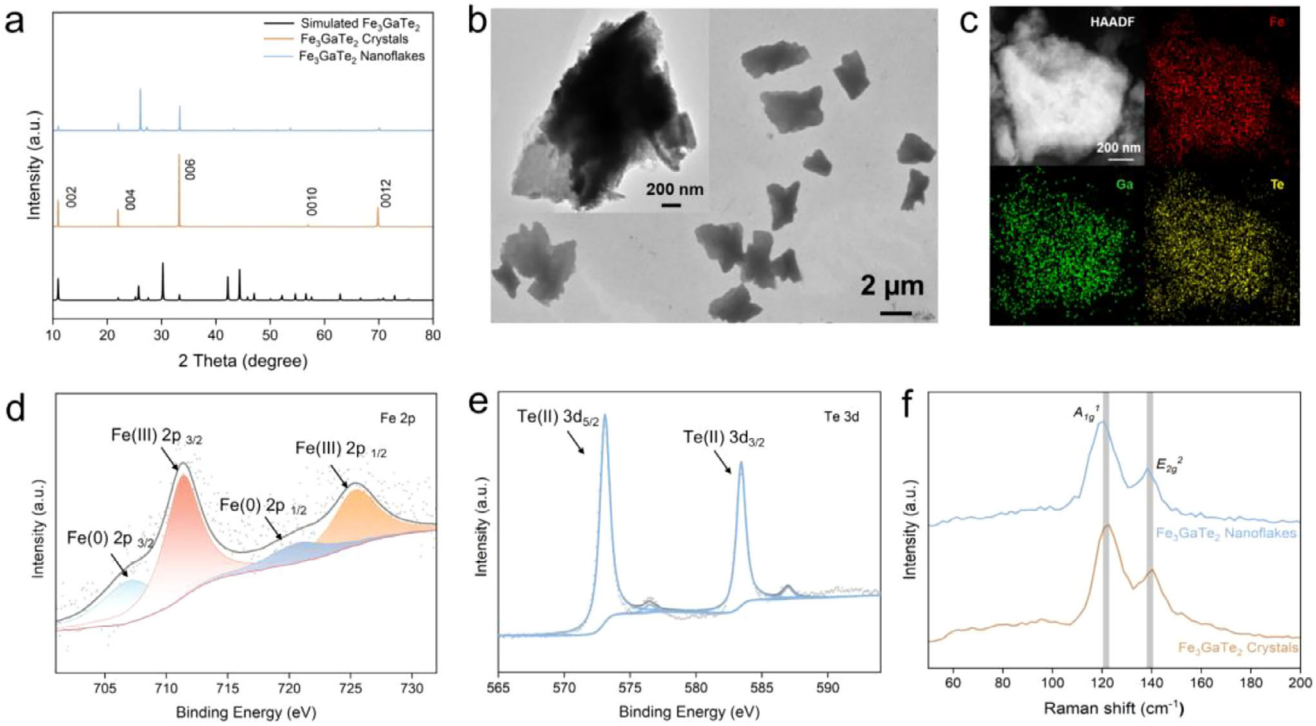

Figure 2. a) XRD patterns of Fe_3GaTe_2 crystals and Fe_3GaTe_2 nanoflakes. b) SEM and TEM images of the exfoliated Fe_3GaTe_2 nanoflakes. c) HAADF-EDS images of the Fe_3GaTe_2 nanoflakes. d) Fe and e) Te high-resolution XPS analysis of the Fe_3GaTe_2 nanoflakes. f) Raman image of Fe_3GaTe_2 crystals and the Fe_3GaTe_2 nanoflakes.

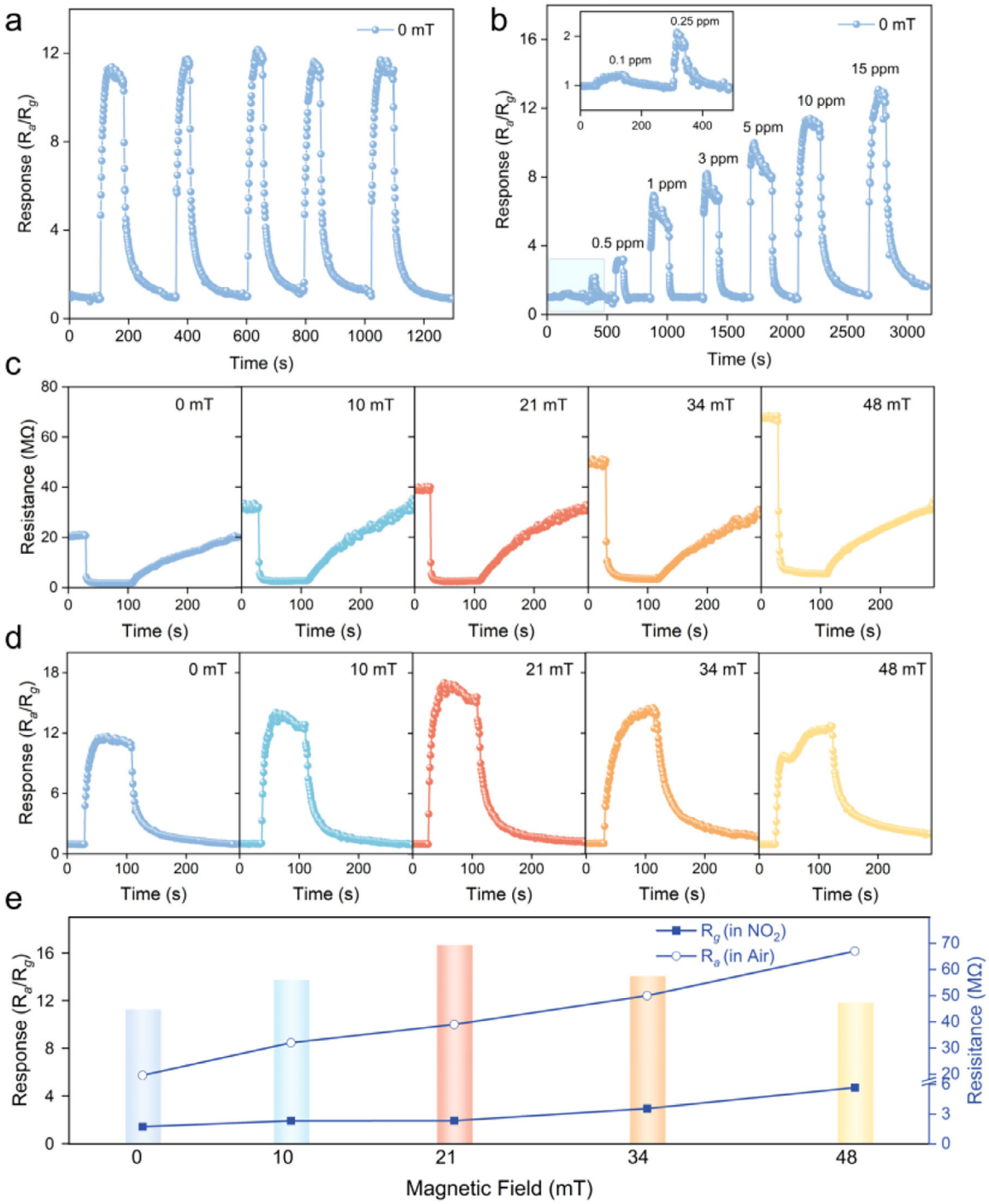

Figure 3. a) Cycle curves for 10 ppm and b) Response curves for 0.1–15 ppm NO_2 of Fe_3GaTe_2 based sensor at room temperature without magnetic field. c) Resistance and response d) curves for 10 ppm NO_2 at room temperature under 0, 10, 21, 34, and 48 mT magnetic field. e) Summary of the response values for 10 ppm NO_2, R_a, and R_g of the sensor under different magnetic field strengths.

Studies on the directional relationship between magnetic fields and sensors have shown that applying a vertical magnetic field provides a more prominent enhancement effect. Simultaneously, in this work, the vertical magnetic field significantly influenced the resistance of sensors. Therefore, a vertical magnetic field was prioritized applying to systematically investigate the impact on the performance of sensors. Here, permanent magnets were chosen to supply the various magnetic fields. The room temperature transient resistance and response curves of the sensor toward 10 ppm NO_2 under different magnetic field intensities at room temperature were presented. All results showed that the typical *p*-type sensing curves consistent with the case of the

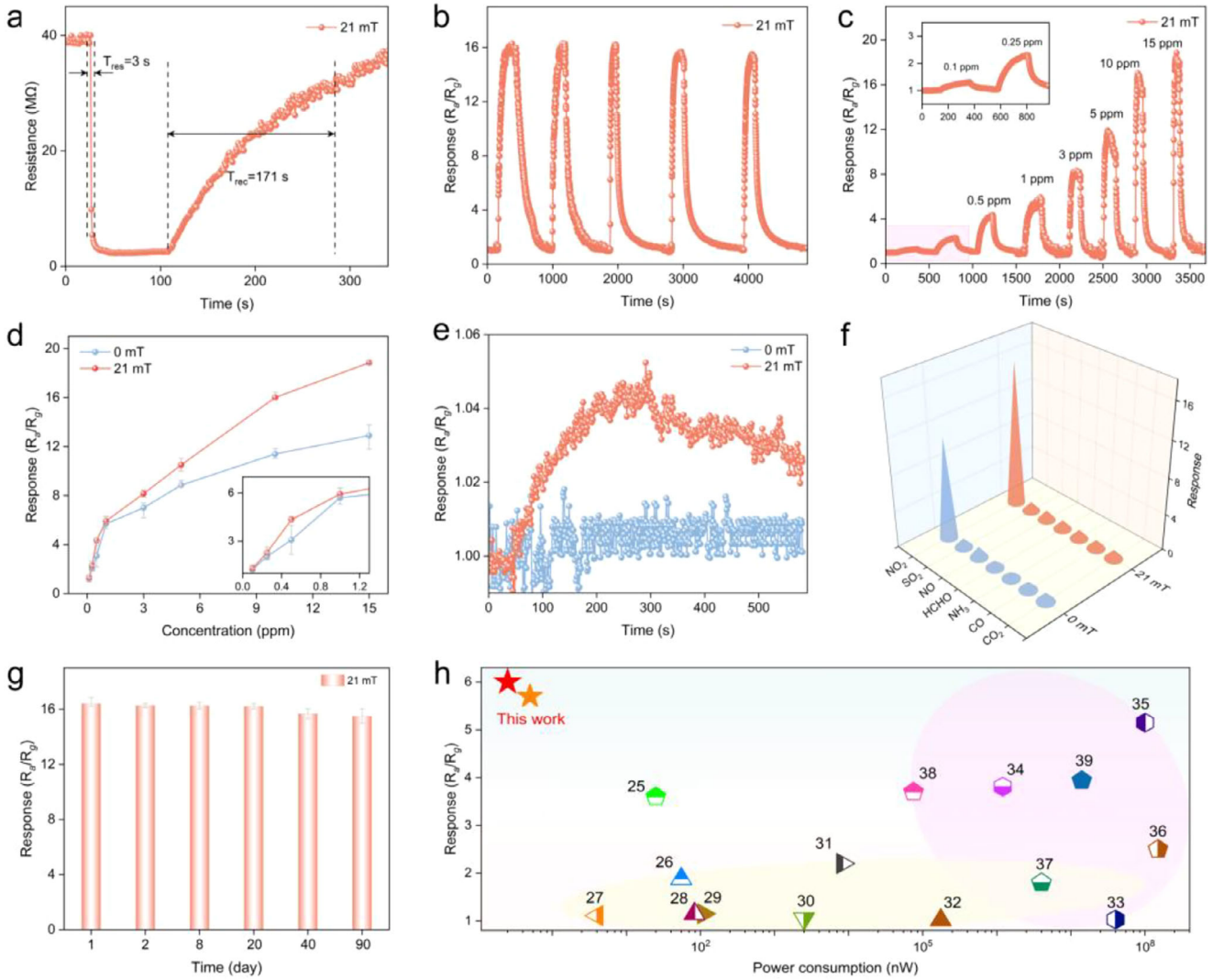

Figure 4. a) Resistance response/recovery characteristics and b) Cycle curves toward 10 ppm NO_2 of Fe_3GaTe_2 based sensor under 21 mT magnetic field at room temperature. c) Response curves under 21 mT and d) Response values under 0 and 21 mT magnetic field toward 0.1–15 ppm NO_2 of the sensor at room temperature. e) Response curves for 0.05 ppm NO_2, and f) Selectivity for 10 ppm NO_2 and common air pollutants gases under 0 and 21 mT magnetic field. g) Long-term stability toward 10 ppm NO_2 under 21 mT magnetic field. h) Graph comparing NO_2 response and power consumption of reported gas sensors.

magnetic field absence. And R_g increased with increasing of magnetic field strength (Figure 3c). The response values exhibited a "hill" trend with increasing magnetic field strength. Under magnetic fields of 0, 10, 21, 34, and 48 mT, the response values for 10 ppm NO_2 were 11.25, 13.73, 16, 14, and 11.8, respectively. Among, the peak response under a 21 mT magnetic field was 1.42 times that without a magnetic field (0 mT) condition (Figure 3d). This trend aligned with the effect of temperature on response, indicating that magnetic fields could effectively modulate the performance of the sensor as an external stimulus. Figure 3e summarized the response values, R_a, and R_g under different magnetic field strengths. As magnetic field intensity increased, both R_a and R_g showed that an upward trend, with the increased amplitude of R_a being much larger than that R_g. This indicated that the magnetic field had a stronger influence on the resistance of the sensor in air than in the NO_2, which might be due to the fact that the gas environment could change the intrinsic magnetism of the material. The material exhibited weaker intrinsic magnetism in NO_2 compared to air. This also explained why the response showed a "hill" pattern under different magnetic field strengths.

Systematic gas sensing performance tests were conducted under 21 mT to validate the reliability of the applied magnetic field. As shown in **Figure** 4a, the response time (T_{res}) of the sensor toward 10 ppm NO_2 is 3 s, with a recovery time (T_{rec}) of 171 s under a 21 mT magnetic field. Figure 4b confirmed the excellent cyclic stability of the sensor under a 21 mT magnetic field. The response curves (Figure 4c) and linear fitting (Figure S4c, Supporting Information) results of the sensor to 0.1–15 ppm NO_2 under a 21 mT magnetic field shown that the sensor exhibited a higher linear relationship compared to that without magnetic, indicating enhanced sensitivity for NO_2 sensing. Specifically, toward 0.1–1 ppm NO_2, the sensitivity of the sensor was 5.12

Table 1. Comparison of power consumption and sensing performance for 1 ppm NO2 of chemiresistive gas sensors.

Materials	Temperature	External field	Power [nW]	Response [R_a/R_g]	Refs.
$CsCu_2I_3$	RT	–	25	3.6	[25]
$FA_{0.83}Cs_{0.17}PbI_3$	RT	–	55	1.88	[26]
Sb_2Se_3	RT	–	4	1.11	[27]
WS_2@MTCNFs	RT	–	83	1.15	[28]
WS_2_Co-N-HCNCs-700	RT	–	110	1.15	[29]
NbS_2	RT	–	2500	1.05	[30]
MoS_2 nanosheets	RT	–	8300	2.2	[31]
M_Fe/PANI:PSS	RT	–	1 75 000	1.018	[32]
WS_2/Au/ZnO	RT	Light	40 000 000	1.03	[33]
C-InSe	RT	Light	1200 000	3.81	[34]
CuO/MoS_2	RT	Light	100 000 000	5.15	[35]
Pt/Nb/In_2O_3	94 °C	MEMS heater	150 000 000	2.5	[36]
TeO_2 doped ZnO	100 °C	MEMS heater	4 000 000	1.8	[37]
In_2O_3	160 °C	MEMS heater	75 000	3.7	[38]
SnO_2-InO_x	200 °C	MEMS heater	14 000 000	3.94	[39]
Fe_3GaTe_2	RT	–	0.5	5.7	This work
Fe_3GaTe_2	RT	Magnetic field	0.25	6	This work

*For ease of comparison, uniformly adopt the performance of 1 ppm NO_2 as the standard, and the response adopt R_a/R_g. The sensor power is directly provided by the original text or obtained from the formula of $P = I^2*R$ or $P = U^2/R$ based on the data provided in the text.

under a 21 mT magnetic field, while that without a magnetic field was 4.93. It was worth noting that the magnetic field significantly enhanced the gas sensitivity performance with NO_2 concentration higher than 1 ppm. With the concentration increases, the response value tends to saturate in the absence of magnetic field; but with the addition of an external magnetic field, the saturation tendency diminishes and the response values increase significantly (Figure 4d), which indicates that the external magnetic field plays a dominant role. Enhanced sensitivity implies a reduced practical limit of detection (pLOD). There was a detectable response of 1.043 for 50 ppb NO_2 under a 21 mT magnetic field at room temperature, but no change in response curve without a magnetic field (Figure 4e). This achieves a practical detection limit of 53 ppb matching the U.S. EPA's annual average safety threshold for ambient NO_2.

Additionally, selectivity was evaluated to determine the relative response of NO_2 to other common air pollutants gas (Figure 4f). The sensor was exposed to 10 ppm for NO_2, SO_2, NO, HCHO, NH_3, CO and 0.1% CO_2. The sensors based on Fe_3GaTe_2 have excellent specificity for NO_2. By utilizing an external magnetic field, the need for an external heat source/light source is eliminated, which reduces power consumption while improving gas sensing performance. The long-term stability of the Fe_3GaTe_2 based sensor under 21 mT magnetic field is shown in Figure 4g. It could be observed that the response values of the Fe_3GaTe_2 based sensor have only a slight fluctuation, indicating that the sensor has a superior long-term stability under the action of a 21 mT magnetic field.

The fabricated sensors based on Fe_3GaTe_2 in this work exhibit remarkable sensitivity to NO_2 at room temperature with low power consumption (Figure 4h).[25–39] For ease of comparison, we uniformly adopt the performance of 1 ppm NO_2 as the standard (**Table 1**). Thus, Fe_3GaTe_2 nanoflakes demonstrate superior room temperature NO_2 sensing properties including high response, low detection limit, and excellent cyclic stability. External magnetic fields offer an effective and promising strategy to enhance the sensor performance including boosting response, lowering detection limits, and reducing power consumption.

2.3. Mechanism

The working mechanism of 2D material-based chemiresistive gas sensors is usually proposed based on the space charge layer model.[40–43] The sensing material interacts with the gas for electron transfer, causing a change in the resistance of the material to recognize the target gas. In our work, the sensor exhibits the typical p-type sensing perporties and the R–T curve was displayed in Figure S5 (Supporting Information). The core of the sensing mechanism is that NO_2 molecules could capture the electrons on the surface of Fe_3GaTe_2 when contacting with the sensor. Upon NO_2 removing, these electrons would be released back into the material. In order to explore the reaction mechanism in depth, we performed quasi in situ XPS tests on the material in the NO_2. The total XPS results showed that the changes were insignificant regardless of NO_2 presence (**Figure 5**a), indicating the overall chemical states of the material have not changed significantly and exhibit structural stability. The high-resolution Fe 2p results were shown in Figure 5b, the peaks had an overall shift to high energy when the material was exposed to NO_2, suggesting that the material loses electrons compared without NO_2, which is consistent with our previous speculation. Te 3d has no significant change in chemical state in NO_2 (Figure 5c), suggesting that Fe acts as the main electron donor and serves as the main response site for NO_2 sensing. To confirm this point, we conducted theoretical calculations on different adsorption sites of the Fe_3GaTe_2 for NO_2 (Figure S6, Supporting Information). The Bader charge results showed that the charge transfer between the material and

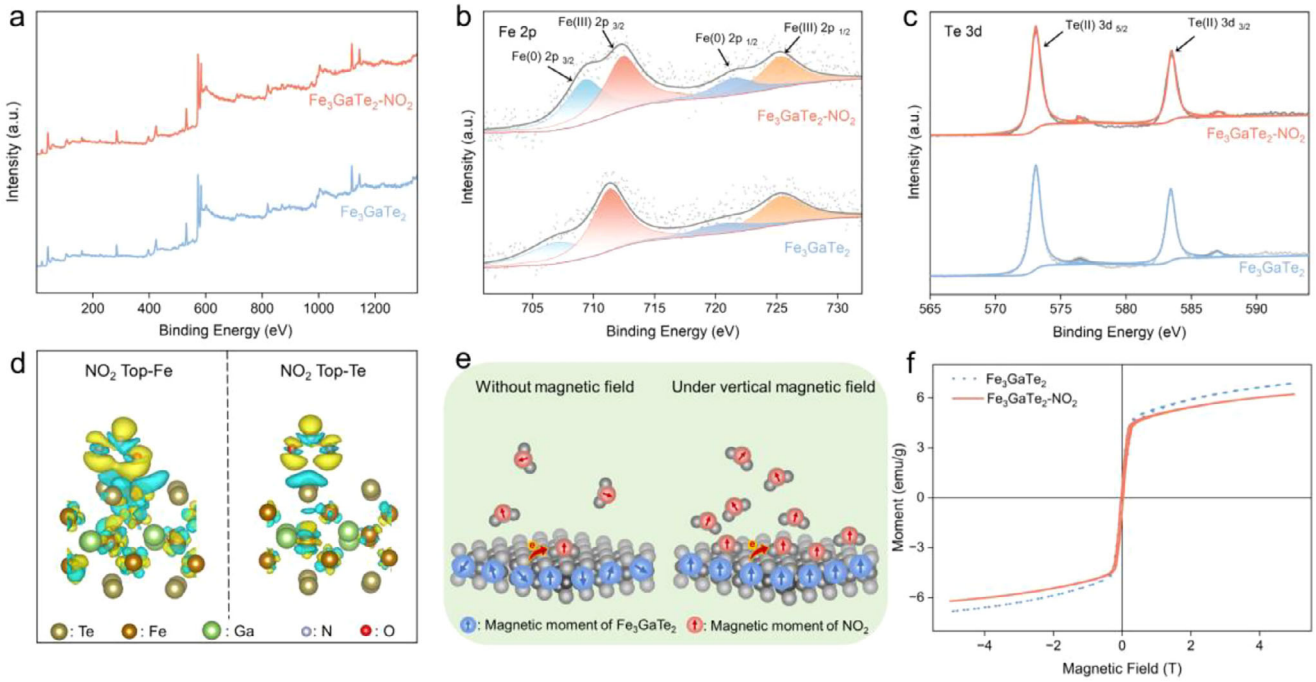

Figure 5. a) Total, b) Fe 2p, and c) Te 3d XPS curves for Fe_3GaTe_2 and Fe_3GaTe_2-NO_2. d) Charge Difference Density of NO_2 on the top-Fe and top-Te sites of Fe_3GaTe_2 (Yellow and blue colors indicate the electron accumulation and depletion, respectively. The isosurface is set to 0.02e $Å^{-3}$). e) The schematic of magnetic moment and NO_2 adsorption changing with/without magnetic field. f) Field-dependent magnetization at 300 K for Fe_3GaTe_2 in air and in NO_2.

NO_2 at the Top-Fe site (0.61 e) was stronger than that at the Top-Te site (0.42 e). The results of Charge Difference Density indicated that, under the same isosurface setting, the electron transfer between the Fe_3GaTe_2 and NO_2 at the Top-Fe site was significantly stronger than at the Top-Te site (Figure 5d). Consistent with the XPS results, confirming the mechanism we proposed.

The mechanism of magnetic field-enhanced gas adsorption capacity of magnetic materials can be understood in terms of multidimensional synergy. First, the magnetic field can induce an orderly arrangement of magnetic moments inside the magnetic material, and a uniform and enhanced localized magnetic field is formed on the surface of the material. Compared with the disordered state, the magnetically enhanced surface shows a much stronger ability to trap paramagnetic NO_2 molecules. This further increases the probability of NO_2 colliding with the Fe_3GaTe_2 surface (Figure 5e). This directly explains the decreased pLOD under 21 mT magnetic field. The retention time of the gas molecules on the surface of the material is also increased, which is why the complete recovery speed of the sensor slows down as the magnetic field enhancement, it is the currently proposed port docking mechanism.[11] Second, the carriers are redistributed by the Lorentz force under the action of the magnetic field, which changes the interfacial barrier and improves the gas sensing performance of the sensor.[14] Meanwhile, the Lorentz force leads to enhanced scattering of charge transport, and the existence of an interlayer potential barrier between adjacent nanoflakes, which will polarize the surface charge distribution and increase the resistance of charge carriers crossing the interlayer gap. Macroscopically, the base resistance R_a of the sensor increases with the enhancement of the magnetic field. Importantly, we propose that the improvement in the gas sensing properties of the material may also be related to the change in magnetic properties under different atmospheres, and in situ M–S curves of the Fe_3GaTe_2 with NO_2 were performed. When NO_2 molecule is adsorbed on Fe site, the strong electronegativity of NO_2 could capture electron from Fe site, leading to a change in the local magnetic moment of Fe atom. This change in local magnetic moment further propagates to the entire material system, reducing the Ms of Fe_3GaTe_2 from 6.86 emu g^{-1} in air to 6.19 emu g^{-1} in NO_2 (Figure 5f). This results in a distinct difference in the magnetic response of the material between air and NO_2. Based on these, we propose a novel mechanism to explain the magnetic field-enhanced sensing performance, namely GAMVE. The core role of Fe_3GaTe_2 in GAMVE lies in its unique property of Ms decreasing in NO_2 atmosphere. Combining with the gas adsorption process, the effect of the magnetic field on resistance changes in NO_2 is weaker than that in air. Consequently, the rate of change in resistance during the sensing increases accordingly, which in turn improves the gas sensing performance, consistent with the results of the sensing tests. It provides a novel research perspective and idea to reveal the relationship between material magnetism and gas sensing. Although, the interaction between gas molecule adsorption and magnetism in this study exhibits subtle variations rather than a strong 0-to-1 switching effect, the proposed GAMVE will help elucidate the intrinsic mechanism underlying the electrical and magnetic changes in this system upon gas exposure, providing theoretical support for the development of next-generation gas sensing technologies.

3. Conclusion

In summary, we have utilized the unique advantages of the 2D room-temperature magnetic material Fe_3GaTe_2 to achieve high-performance and low-power detection of NO_2 at room temperature without an external heat or light source, which has not been reported in previous gas sensor studies. High quality single crystal Fe_3GaTe_2 was synthesized using CVT, and the nanoflakes were obtained by ultrasonically assisted liquid-phase exfoliation in a water/ethanol mixed solvent. The Fe_3GaTe_2 nanoflakes sensor exhibited an enhanced NO_2 response (S = 16) to 10 ppm NO_2 under 21 mT magnetic at room temperature, which was 1.4 times higher than that without magnetic field. Meanwhile, a lower actual detection limit (50 ppb) and a low-power consumption (0.25 nW) can be observed by applying a 21 mT magnetic field. This study revealed for the first time that the magnetic field-enhancing effect for gas sensing is not only attributed to the ordering of magnetic moments and the redistribution of carriers, but primarily originates from GAMVE. This solves the trade-off between performance and energy for conventional materials and provides a new strategy for developing next-generation gas sensors.

4. Experimental Section

Growth of High-Quality Bulk Single Crystals of Fe_3GaTe_2: The synthesis method of Fe_3GaTe_2 with high-quality single crystals was the chemical vapor transport (CVT) method.[43] High-purity Fe, GaTe, and Te powders were mixed in a molar ratio of 3: 1: 1, sealed with iodine beads (as the vapor transport agent) in a 12 cm evacuated quartz tube. The evacuated quartz tube was placed horizontally in a dual-zone tube furnace with a heating rate of 2 °C min^{-1}, and maintained at 750 °C (hot end) and 700 °C (cold end) for 6 days. After natural cooling to room temperature, the high-quality single crystals of Fe_3GaTe_2 were obtained.

Fe_3GaTe_2 Nanoflakes by Liquid-Phase Exfoliation Method: The Fe_3GaTe_2 nanoflakes dispersion was prepared by the liquid-phase exfoliation method, as shown in Figure 1. First, the bulk Fe_3GaTe_2 crystals were ground to reduce the thickness and lateral dimensions of the materials. The ground material was then dispersed in a mixed solvent of water and ethanol (the volume ratio of 3: 1) at a concentration of 0.5 mg mL^{-1}. While maintaining an ice-water bath, it was subjected to continuous probe sonication with 105 W output power (150 W × 70%) for 30 min using a pulsed mode (10 s on / 10 s off) to prevent excessive heating. This ultrasonic treatment facilitates the expansion of interlayer spacing and weakening of interlayer van der Waals (vdW) forces, resulting in the exfoliation of nanoflakes. The resulting dispersion is referred to as the Fe_3GaTe_2 nanoflakes dispersion and Fe_3GaTe_2 nanoflakes powders were obtained by freeze-drying.

Material Characterizations: The crystalline phases were characterized by XRD (BRUKER D8 ADVANCE) with Cu Kα radiation (λ = 1.54 Å) in a 2θ range of 10°–80°. The morphologies of the samples were observed by scanning electron microscope (ZEISS Ultra 55) and transmission electron microscopy (FEI Talos F200X). The composition and chemical state of the samples were investigated by XPS (Thermo Fisher NEXSA). Raman spectra were tested at 532 nm excitation wavelength (Renishaw inVia). X-ray photoelectron spectroscopy (XPS) was obtained by Thermo SCIENTIFIC ESCALAB Xi+, and using C1s at 284.8 eV as a reference. Magnetometry measurements and resistance-temperature (R–T) curve were carried out with the Quantum Design PPMS.

Fabrication and Measurement of the Gas Sensor: A 10 µL dispersion of Fe_3GaTe_2 nanoflakes was drop-cast onto Ag/Pd interdigitated electrodes (IDEs) with a 200 µm electrode gap. The sensor was subsequently dried and could then be used for gas-sensing measurements. The real-time resistance value of the sensors was monitored by a source meter (Keithley 2450) at room temperature (≈25 °C, 30% RH). The external magnetic field was achieved by placing the sensor between two identical magnets, and the magnetic field intensity was adjusted by altering the magnet parameters. The gas preparation details are shown in Supporting Information. Mathematically, the response (S) is denoted as $S = R_a/R_g$ to NO_2, where R_a and R_g represent the resistance of the sensor in air and the target gases, respectively.

Supporting Information

Supporting Information is available from the Wiley Online Library or from the author.

Acknowledgements

This work was supported by Guangdong Basic and Applied Basic Research Foundation (2025A1515012116, 2023B1515020112), Scientific Research Program of Guangdong Provincial Laboratory of Southern Ocean Science and Engineering (Zhuhai) (No. SML2024SP020), Department of Science and Technology of Guangxi Province (No. AB25069461), the National Natural Science Foundation of China (62571326, 52322108), and Guangdong Provincial Key Laboratory of Optical Information Materials and Technology (2023B1212060065). The 111 Project. Calculations were made at Bianshui Riverside Supercomputing Center (BRSC).

Conflict of Interest

The authors declare no conflict of interest.

Data Availability Statement

The data that support the findings of this study are available from the corresponding author upon reasonable request.

Keywords

Fe3GaTe2, gas sensing, magnetic field, magnetic variation, room temperature

Received: October 9, 2025
Revised: November 23, 2025
Published online:

[1] M. J. Cooper, R. V. Martin, M. S. Hammer, P. F. Levelt, P. Veefkind, L. N. Lamsal, N. A. Krotkov, J. R. Brook, C. A. McLinden, *Nature* **2022**, *601*, 380.
[2] A. V. Agrawal, A. Y. Polyakov, J. Eriksson, T. J. Antosiewicz, T. O. Shegai, *Small Struct.* **2025**, *6*, 2400409.
[3] X. Zhao, Z. Xu, Z. Zhang, J. Liu, X. Yan, Y. Zhu, J. P. Attfield, M. Yang, *Nature Commun.* **2025**, *16*, 182.
[4] P. M. Bulemo, D.-H. Kim, H. Shin, H.-J. Cho, W.-T. Koo, S.-J. Choi, C. Park, J. Ahn, A. T. Güntner, R. M. Penner, I.-D. Kim, *Chem. Rev.* **2025**, *125*, 4111.
[5] Z. Chen, J. Wang, X. Liu, Y. Wang, J. Shen, J. Li, X. Liu, X. Li, W. Pei, Y. Guo, G. Shi, H. Li, A. M. U. Siddiqui, N. F. de Rooij, L. Jiang, G. Zhou, *J. Am. Chem. Soc.* **2025**, *147*, 3478.
[6] H. Liang, X. Guo, L. Guo, S. Liu, Q. Zhan, H. Yang, H. Li, N. F. de Rooij, Y. K. Lee, P. J. French, Y. Wang, G. Zhou, *Adv. Funct. Mater.* **2023**, *33*, 2215099.

[7] J. Chang, C. Qin, W. Guo, L. Zhu, Y. Zhang, Y. Wang, J. Cao, *Sensor. Actuat. B: Chem.* **2023**, *385*, 133633.
[8] R. Li, L. P. Qiu, S. Z. Cao, Z. Li, S. L. Gao, J. Zhang, S. Ramakrishna, Y. Z. Long, *Adv. Funct. Mater.* **2024**, *34*, 2316725.
[9] Y. Sun, H. Lv, H. Yao, Y. Gao, C. Zhang, *Carbon Energy* **2024**, *6*, 575.
[10] J. Y. Lin, W. M. Xie, X. L. He, H. C. Wang, *Applied Physics A* **2016**, *122*, 801.
[11] H. Sun, M. Cao, P. Zhang, X. Tian, M. Lu, L. Du, K. Xue, G. Cui, *ACS Sens.* **2022**, *7*, 1903.
[12] Z. Zhang, J. Cao, S. Wang, Z. Sun, J. Li, *Adv. Funct. Mater.* **2023**, 2305253.
[13] J. Cao, Z. Zhang, S. Wang, Z. Sun, J. Li, Y. Wang, X. Xu, Z. Ye, H. Zhang, *ACS Sens.* **2024**, *9*, 4777.
[14] P. Rudra, N. V. Dambhare, V. Srihari, S. Das, A. K. Rath, D. Saha, S. Mondal, *ACS Appl. Nano Mater.* **2024**, *7*, 14331.
[15] J. Chang, Y. Gao, Z. Hou, Y. Wang, *Current Chinese Science* **2024**, *05*, 22102981359015.
[16] Y. Shi, L. Ni, Z. Wang, M. Chen, L. Feng, *Coordin. Chem. Rev.* **2024**, *505*, 215691.
[17] Z. Chen, J. Wang, D. Pan, Y. Wang, R. Noetzel, H. Li, P. Xie, W. Pei, A. Umar, L. Jiang, N. Li, N. F. de Rooij, G. Zhou, *ACS Nano* **2018**, *12*, 2521.
[18] M. Wang, B. Lei, K. Zhu, Y. Deng, M. Tian, Z. Xiang, T. Wu, X. Chen, *NPJ 2D Material. Appl.* **2024**, *8*, 22.
[19] C. Liu, S. Zhang, H. Hao, H. Algaidi, Y. Ma, X. X. Zhang, *Adv. Mater.* **2024**, *36*, 2311022.
[20] Z. Li, H. Zhang, G. Li, J. Guo, Q. Wang, Y. Deng, Y. Hu, X. Hu, C. Liu, M. Qin, X. Shen, R. Yu, X. Gao, Z. Liao, J. Liu, Z. Hou, Y. Zhu, X. Fu, *Nat. Commun.* **2024**, *15*, 1017.
[21] G. Zhang, F. Guo, H. Wu, X. Wen, L. Yang, W. Jin, W. Zhang, H. Chang, *Nat. Commun.* **2022**, *13*, 5067.
[22] X. Liang, F. Chen, L. Yang, T. Yang, P. Xiao, Y. Liu, Z. Wang, W. Xiao, *J. Phys. Condens. Matter.* **2025**, *37*, 155001.
[23] M. Yang, L. Wang, G. Hu, X. Chen, P. L. Gong, X. Cong, Y. Liu, Y. Yang, X. Li, X. Zhao, X. Liu, Optical identification of interlayer coupling of graphene/MoS_2 van der Waals heterostructure, *Nano Res.* **2021**, *14*, 2241.
[24] W. Huang, X. Zhuang, F. S. Melkonyan, B. Wang, L. Zeng, G. Wang, S. Han, M. J. Bedzyk, J. Yu, T. J. Marks, A. Facchetti, *Adv. Mater.* **2017**, *29*, 1701706.
[25] S. J. Kim, G. B. Nam, Y. J. Kim, T. H. Eom, J. E. Ryu, H. J. Kim, H. J. Lee, H W. Jang, *Nano Lett.* **2025**, *25*, 2894.
[26] Z. Lu, C. Lou, A. Cheng, J. Zhang, J. Sun, *J. Alloy. Compound.* **2022**, *919*, 165831.
[27] Y. B. Kim, S. H. Jung, D. S. Kim, N. G. Deshpande, H. W. Suh, H. H. Lee, J. H. Choi, H. S. Lee, H. K. Cho, *Adv. Funct. Mater.* **2021**, *31*, 2102439.
[28] J.-H. Cha, S.-J. Choi, S. Yu, I.-D. Kim, *J. Mater. Chem. A* **2017**, *5*, 8725.
[29] W.-T. Koo, J.-H. Cha, J.-W. Jung, S.-J. Choi, J.-S. Jang, D.-H. Kim, I.-D. Kim, *Adv. Funct. Mater.* **2018**, *28*, 1802575.
[30] Y. Kim, K. C. Kwon, S. Kang, C. Kim, T. H. Kim, S. P. Hong, S. Y. Park, J. M. Suh, M. J. Choi, S. Han, H. W. Jang, *ACS Sens.* **2019**, *4*, 2395.
[31] H. H. Hau, T. T. H. Duong, N. K. Man, T. Thi Viet Nga, C. Thi Xuan, D. Thi Thanh Le, N. Van Toan, C. M. Hung, N. Van Duy, N. Van Hieu, N. D. Hoa, *Sensor. Actuat. A: Phys.* **2021**, *332*, 113137.
[32] S. G. Kim, J. Jun, J. S. Lee, J. Jang, *J. Mater. Chem. A* **2019**, *7*, 8451.
[33] C. Yao, L. Wu, H. Li, N. Xu, J. Sun, J. Wu, *Appl. Surf. Sci.* **2022**, *584*, 152508.
[34] L. Zhang, Q. Hao, J. Liu, J. Zhou, W. Zhang, Y. Li, *Chem. Eng. J.* **2022**, *446*, 136937.
[35] H. Bai, H. Guo, C. Feng, J. Wang, B. Liu, Z. Xie, F. Guo, D. Chen, R. Zhang, Y. Zheng, *Sensor. Actuat. B: Chem.* **2022**, *368*, 132131.
[36] W. J. Zhao, D. Xu, Y. S. Chen, X. Wang, Y. B. Shi, A *Sensors* **2019**, *19*, 3719.
[37] Y. Nagarjuna, Y. J. Hsiao, *Sensor. Actuat. B: Chem.* **2024**, *401*, 134891.
[38] H. Mei, F. Zhang, T. Zhou, T. Zhang, *Sensors* **2024**, *24*, 7188.
[39] Z. H. Shi, Y. J. Hsiao, S. C. Wang, W. C. Tien, *J. Electrochem. Soc.* **2023**, *170*, 027509.
[40] Y. Niu, J. Zeng, X. Liu, J. Li, Q. Wang, H. Li, N. F. de Rooij, Y. Wang, G. Zhou, *Adv. Sci.* **2021**, 2100472.
[41] Shi, L. Ni, Z. Wang, M. Chen, L. Feng, *Chem. Rev.* **2024**, *505*, 215691.
[42] Z. Fu, Y. Chang, Z. Chen, H. Xie, Y. Feng, F. Wang, Y. Wang, H. Li, Y. Gao, T. Ren, P. J. French, A. M. Umar Siddiqui, G. Zhou, *Small* **2025**, 2411264.
[43] H. Algaidi, C. Zhang, Y. Ma, C. Liu, A. Chen, D. Zheng, X. Zhang, *APL Mater.* **2024**, *12*, 011124.